ADVANCED FUNCTIONAL MATERIALS
www.afm-journal.de

Shape-Controlled $NaTaO_3$ by Flux-Mediated Synthesis

Kootak Hong, Shaun Tan, Matthew J. McDermott, Tianyi Huang, Finn Babbe, Tim Kodalle, Max Gallant, Sehun Seo, Francesca M. Toma, Kristin A. Persson, Yang Yang, and Carolin M. Sutter-Fella**

$NaTaO_3$ is a stable and wide bandgap n-type semiconductor material with many different applications. Here, a flux-mediated synthesis method is presented for $NaTaO_3$ resulting in highly distinctive, substrate covering shapes via precursor chemistry variation at comparatively low temperatures. It is found that the microstructure of the resulting $NaTaO_3$ films can be varied from nanocubes to smooth thin films. These shapes and surface chemistries can be correlated by employing density functional theory calculations and surface sensitive X-ray photoemission spectroscopy. This study provides guidance on how to synthesize the material and tailor its shape and surface termination for different applications. Finally, as a proof of concept of one possible application, $NaTaO_3$ is applied to perovskite solar cells as the electron transport layer, resulting in conversion efficiencies of >19%. This study provides a new strategy for designing ternary oxide thin films for renewable energy applications.

1. Introduction

Metal oxides are highly versatile and can appear as semimetals, semiconductors, or insulators with a wide range of functionalities with unique tunability of physicochemical properties via control of their elemental composition.[1–4] Traditionally, complex metal oxides are prepared by the ceramic (or solid-state) method, which involves several cycles of grinding and heating, long calcination steps at high temperatures (well above 1000 °C), and intermediate wet milling processes.[5–7] The high temperatures and surface areas are needed to increase the reaction rate and reduce the diffusion path. Reactions are often slow because solid-state reactions solely take place at the interface of the reactants.[2] In addition, the final phase often contains unwanted impurity phases. For thin film device applications, the high reaction temperatures are not compatible with device architectures that contain substrates pre-coated with functional materials such as the transparent conducting oxide fluorine-doped tin oxide (FTO).

Among other synthetic techniques, flux-mediated synthesis methods have been widely used to fabricate high-quality complex oxides with excellent phase-homogeneity at relatively low temperatures, which have made a significant impact on renewable energy applications.[1,2] In a flux-mediated synthesis, an inorganic salt acts as a molten-salt solvent by heating it above its melting point. It helps to dissolve solid inorganic reactants and facilitates crystallization and crystal growth well beyond the normal melting point of the final material.[8,9] Flux-mediated synthesis enables synthetic flexibility to tune shape, feature size, and surfaces, as well as composition of complex oxides.[1,2,10]

To this end, the majority of research employing flux-mediated synthesis of oxides has focused on the growth of single-crystals and nanocrystals that are typically not on a support substrate. Although post-processing of nanocrystals into thin films is possible it is often hampered by morphological defects, trap states in the nanoparticle network, and poor physical contact with the adjacent layers.[11–15] The requirement for complex oxides to be incorporated in optoelectronic thin film devices is their formation on a substrate, often coated with FTO that limits the maximum annealing temperature to 700 °C.[16]

In order to exploit the advantages of flux mediated synthesis of metal oxides and apply them to devices it is necessary to

K. Hong, F. Babbe, S. Seo, F. M. Toma
Chemical Sciences Division
Lawrence Berkeley National Laboratory
Berkeley, CA 94720, USA

K. Hong
Department of Materials Science and Engineering
Chonnam National University
Gwangju 61186, Republic of Korea

S. Tan, T. Huang, Y. Yang
Department of Materials Science and Engineering and California NanoSystems Institute
University of California Los Angeles
Los Angeles, CA 90095, USA
E-mail: yangy@ucla.edu

M. J. McDermott, M. Gallant, K. A. Persson
Department of Materials Science and Engineering
University of California
Berkeley, CA 94720, USA

F. Babbe, S. Seo, F. M. Toma
Liquid Sunlight Alliance
Lawrence Berkeley National Laboratory
Berkeley, CA 94720, USA

T. Kodalle, K. A. Persson, C. M. Sutter-Fella
Molecular Foundry
Lawrence Berkeley National Laboratory
Berkeley, CA 94720, USA
E-mail: csutterfella@lbl.gov

The ORCID identification number(s) for the author(s) of this article can be found under https://doi.org/10.1002/adfm.202206641.

DOI: 10.1002/adfm.202206641

elucidate the formation and correlation of their final properties with the nature of the molten salt. Here, we report not the flux synthesis of particles, but on surface-covering $NaTaO_3$ synthesized at temperatures as low as 600 °C that is one-third of its melting point.[17] $NaTaO_3$ is a promising material for renewable energy applications as recently identified by a data-driven materials discovery effort.[18,19]

We investigate the reaction mechanisms, crystallization pathway, and shape evolution from thin films to truncated pyramids, to nanocubes with dependence on the anion of the sodium salt deployed, using in situ X-ray diffraction analysis. Notably, we find that the precursor composition determines the shape of the $NaTaO_3$, a relationship that is supported by surface energy and phase equilibria calculations from density functional theory (DFT). While the large surface-to-bulk ratio shapes are highly desirable for photocatalytic applications, superior function is found in perovskite solar cells if the $NaTaO_3$ forms a thin film. By elucidating the formation mechanism of the ternary oxide and resulting surface chemistries, our findings provide a promising approach to tailor ternary metal oxides for photo-driven applications.

2. Results and Discussion

The flux-mediated synthesis of $NaTaO_3$ was accomplished with several precursor combinations, including Ta metal and amorphous tantalum oxide (TaO_x) thin films as a Ta source, and four different Na-containing salts ($NaNO_3$, CH_3COONa (NaAc), NaCl, and $Na_2S_2O_3$), with dual function, acting as a source of Na and the reactive flux. It is well known that $NaNO_3$, NaAc, NaCl, $Na_2S_2O_3$, and Na_2SO_4 are representative Na-containing precursors to synthesize $NaTaO_3$.[20–24] Among the Na-containing salts, Na_2SO_4 was excluded from this work due to its low solubility in ethylene glycol. After spin-coating a Na-containing solution onto Ta or TaO_x thin films, the samples were dried, and then annealed at 600 °C for 30 min (schematic **Figure 1**a, see Experimental section for details), which is a significantly shorter annealing period at a relatively low temperature when compared to a typical solid-state approach (10 h at 1200 °C) and to the melting temperature of $NaTaO_3$ (1810 °C).[17,25] We note that the deposition sequence is important and if the Na salt is spin-coated first, the Na salt layer melts during the annealing process. This leads to the peeling off of Ta and TaO_x thin films making it difficult to obtain a uniform $NaTaO_3$ layer.

X-ray diffraction (XRD) analysis was performed to investigate the crystal structure and phase purity of the synthesized films. As shown in Figure 1b, we found that phase pure $NaTaO_3$ thin films were successfully synthesized from the combinations of Ta/$NaNO_3$, TaO_x/$NaNO_3$, and TaO_x/NaAc. Ta combinations with NaCl or $Na_2S_2O_3$ did not result in crystalline materials (Figure 1c). We also prepared a sample by drop-casting $NaNO_3$ on Ta metal thin films but found O-rich and other secondary phases possibly due to the Na excess (Figure S1, Supporting Information). This indicates that careful concentration control is important in synthesizing high-quality and phase pure $NaTaO_3$ thin films. The synthesized $NaTaO_3$ materials exhibit very distinct shapes, including nanocubes, truncated pyramids, and flat thin film-like features (Figure 1d–f). These observations are different as compared to $NaTaO_3$ nanoparticles and thin films that are typically reported to have idiomorphic cubic shape.[20,26,27] We also varied the thickness of the precursor Ta and TaO_x thin films to control the growth of $NaTaO_3$ nanocubes, truncated pyramids, and thin films (Figure S2, Supporting Information). It was found that the synthesized $NaTaO_3$ nanocubes, truncated pyramids, and thin films can cover the whole surface of the substrates when the precursor thicknesses are 20–25 nm thick. 2D grazing-incidence wide-angle X-ray diffraction dominantly shows random orientation of $NaTaO_3$ without indication of preferential orientation (Figure 1g–i).

It has been reported that precursors and fluxes determine the shape of the product synthesized by flux-mediated methods.[1,2] Therefore, we want to understand for our specific material system and precursor combinations the crystallization pathways and shape formation and performed in situ XRD measurements in air. **Figure 2** shows 2D contour plots of in situ XRD results and the corresponding observed phases as a function of temperature. The heating/cooling profile is given in Figure S3 (Supporting Information). At the end of the crystallization and cool down, all samples exhibit XRD patterns corresponding to monoclinic $NaTaO_3$ without secondary phases (Figure S4, Supporting Information). The formation onset temperatures of $NaTaO_3$ as well as the crystallization pathways were found to depend on the combination of Ta source and Na salts. The $NaTaO_3$ formation temperature is found to be between 450–550 °C that is significantly lower than its melting temperature of 1810 °C. Observed crystalline phases at the beginning of the annealing are the Na salt ($NaNO_3$ or NaAc) and metallic β-Ta (in case of a pure Ta-precursor) while TaO_x precursors result in amorphous phase. In the Ta/$NaNO_3$ system, the β-Ta peak position first shifted to smaller values with increasing temperature, and then disappeared above 375 °C due to the expansion of the lattice and oxidation, respectively. The diffraction peak for $NaNO_3$ (29.4°) vanished ≈300 °C, which is in good agreement with its melting temperature. Before the formation of $NaTaO_3$ at 450 °C, an intermediate phase, $Na_2Ta_2O_6$, was observed between 325 and 450 °C. Its appearance is attributed to a lower thermodynamic energy barrier height to form $Na_2Ta_2O_6$ instead of $NaTaO_3$, consistent with a previous report.[28] The SEM images of the Ta/$NaNO_3$ sample taken after interrupted annealing at 250, 450, and 550 °C illustrate the shape evolution (Figure 2b). The SEM images suggest that $NaTaO_3$ nanocubes emerge from the $Na_2Ta_2O_6$ phase.

In sharp contrast, combining $NaNO_3$ with TaO_x results in the disappearance of diffraction signals after the $NaNO_3$ peak disappears above 300 °C (Figure 2c). The $NaTaO_3$ phase only emerges at 475 °C. Compared to Ta metal, TaO_x has less active tantalum sources to react with the surrounding Na^+ ions, resulting in direct conversion to $NaTaO_3$ at higher temperature. The obtained SEM images (Figure 2d) show that $NaNO_3$ dewets from the TaO_x surface (250 °C) to form a liquid or liquid-like phase without periodic crystalline structure until $NaTaO_3$ appears at 475 °C exhibiting similarities with truncated pyramids. Lastly, for the TaO_x/NaAc sample, it was found that NaAc decomposes into Na_2O_2 above 400 °C, followed by a temperature window ≈500 °C without crystal phases, i.e., a liquid or liquid-like amorphous phase (Figure 2e). The SEM images of the TaO_x/NaAc sample annealed at different

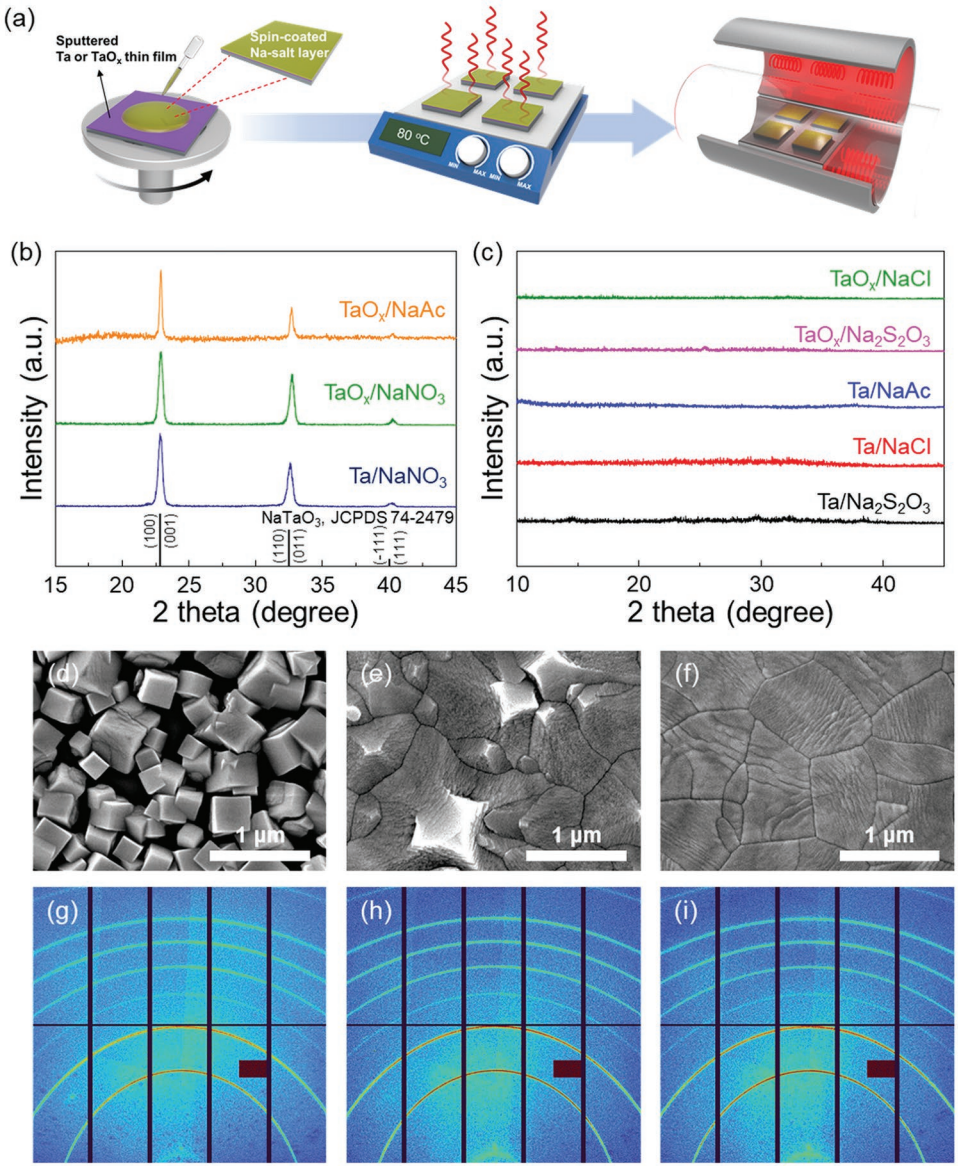

Figure 1. a) Schematic of the Na-solution coating of Ta-containing precursors to facilitate the flux synthesis. b,c) XRD patterns of samples prepared by flux-mediated synthesis method using different precursor combinations. d–f) Plain view-SEM images of $NaTaO_3$ thin films synthesized from the combination of $Ta/NaNO_3$, $TaO_x/NaNO_3$, and $TaO_x/NaAc$, respectively. g–i) Corresponding 2D grazing-incidence wide-angle X-ray diffraction patterns.

temperatures reveal that NaAc fully covers TaO_x before it decomposes and thin film-like $NaTaO_3$ occurs (Figure 2f). Based on these observations, there is evidence that the variation of precursor chemistry (Na salts and Ta sources) determines the reaction pathways, $NaTaO_3$ onset crystallization temperature, and its resulting microstructure or shape. The flux-mediated synthesis is supported by the fact that the diffraction signals completely disappear for the TaO_x precursors indicating absence of any crystalline phase but amorphous or liquid-like phases. Na salts are known fluxing agents and the temperature at which the diffraction signals disappear coincide with the melting point of the Na salt.[1,2] $NaTaO_3$ cannot be synthesized with NaCl or $Na_2S_2O_3$, likely because their melting points are either too high (NaCl) or too low ($Na_2S_2O_3$) to form a molten flux in which the precursor molecules could disperse, dissociate, and diffuse to enable growth of $NaTaO_3$ particles.

The data reported here suggest that the melting temperature of the Na salt, the solubility of the Ta and TaO_x in the Na salt, and the anion of the Na salt each play a role in influencing the crystallization pathway and shape evolution of $NaTaO_3$. To rationalize this observation, we performed surface energy and equilibrium particle shape (Wulff shape) calculations while varying the chemical potential of the constituent elements (Na, Ta, O) to approximate each synthesis environment. Specifically, we constructed a chemical potential diagram for the Na-Ta-O system and identified trends in the Wulff shapes within the $NaTaO_3$ domain on the diagram. This is shown in **Figure 3**a–e, where the Wulff shapes at five representative points (red) within the chemical potential stability domain of $NaTaO_3$ are pictured.

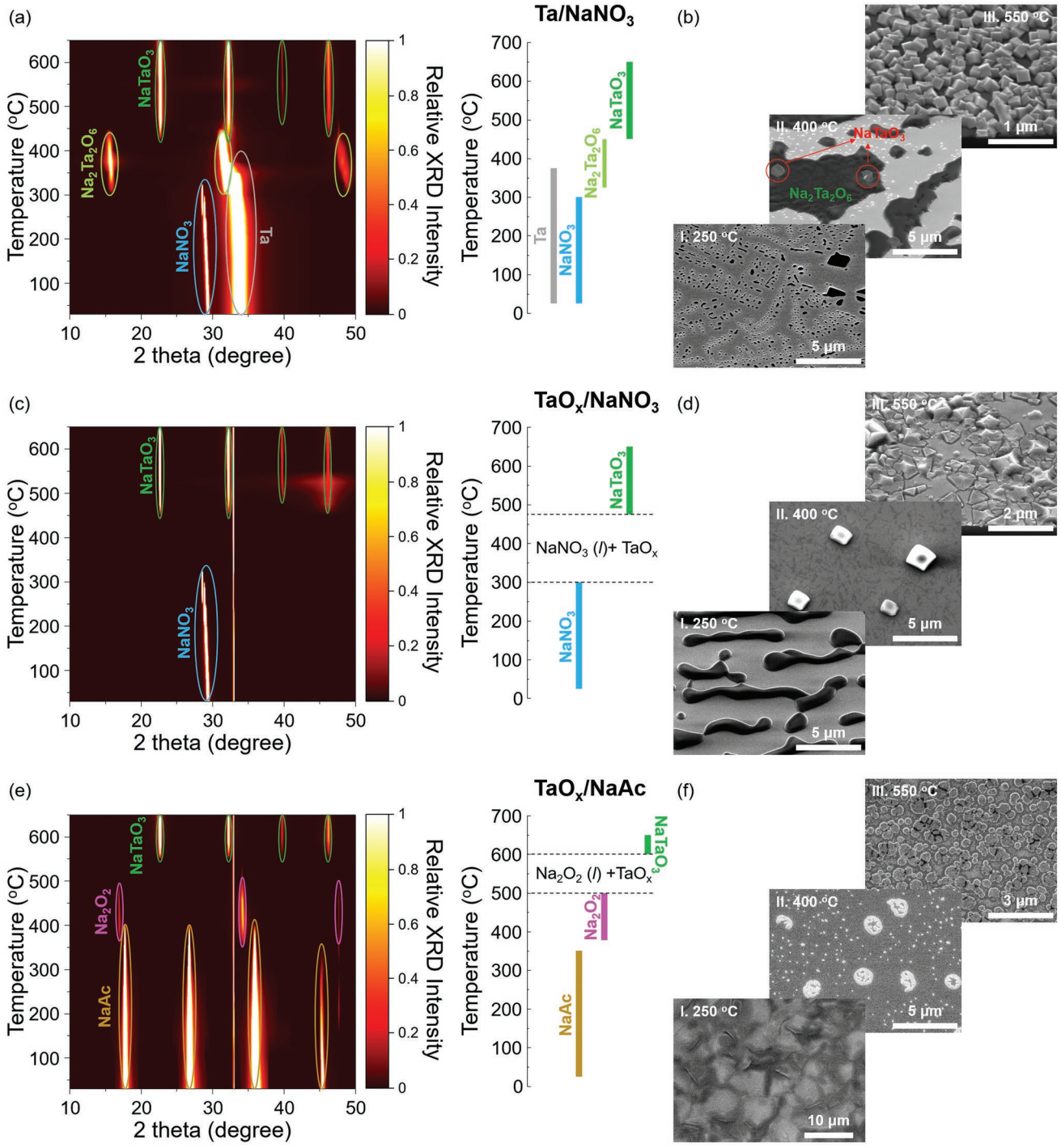

Figure 2. Contour plots of temperature-dependent XRD patterns with observed crystalline phases and SEM images of the samples taken after interrupted annealing at 250, 450, and 550 °C of a,b) Ta/$NaNO_3$, c,d) TaO_x/$NaNO_3$, and e,f) TaO_x/NaAc precursors. The sharp peak at 32.9° is corresponding to a Si substrate (200) peak. Windows without diffraction signals indicate the formation of a liquid-like or amorphous phase of the molten Na-salt and TaO_x.

The point in the upper left, separating the Na_2O_2 and $NaTaO_3$ regions, approximates the conditions encountered during synthesis using the TaO_x/NaAc precursors, which result in a Na_2O_2 flux and a Ta-deficient/Na-rich environment. Under these conditions, the Ta species has a low chemical potential (–12.48 eV), due to its deficiency in the TaO_x compound, and the chemical potential of Na is relatively higher (–2.52 eV) due to its prevalence in the resultant Na_2O_2 flux.

The endpoints given by the upper and lower coordinate points on the $NaTaO_3$/$Na_2Ta_4O_{11}$ border correspond to

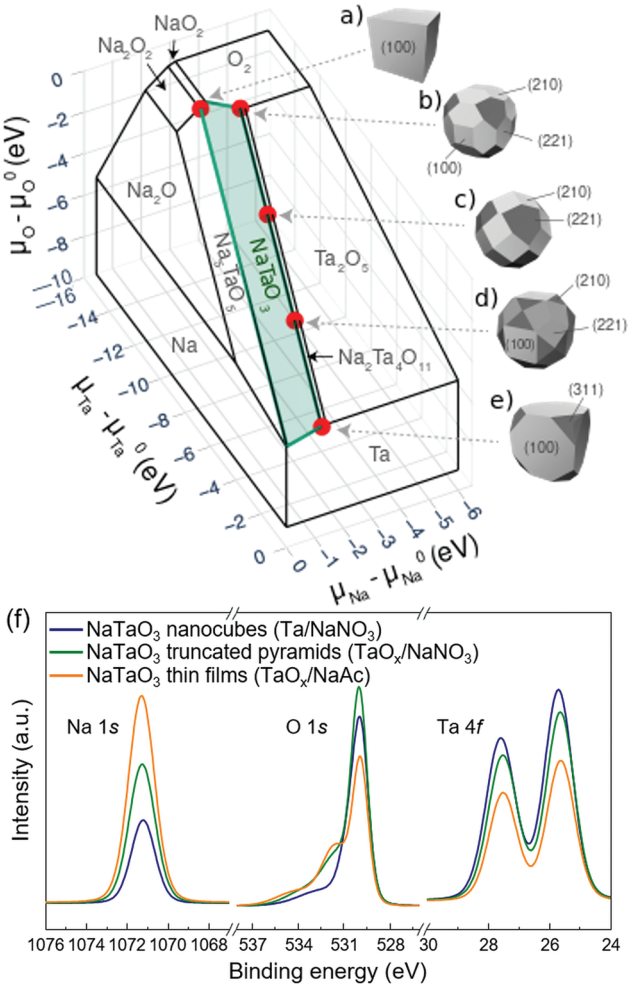

Figure 3. Chemical potential diagram for Na-Ta-O with calculated $NaTaO_3$ Wulff shapes as a function of several points within the $NaTaO_3$ stability domain. The conditions, shown as red coordinate points, range from Na-deficient/Ta-deficient (i.e., O-rich) synthesis conditions (resulting in shapes a,b) to Na-deficient/Ta-rich synthesis conditions (shape e). These are approximations of the synthesis environments when using a) TaO_x/NaAc, b) $TaO_x/NaNO_3$, and e) $Ta/NaNO_3$ precursor combinations. A cubic-like shape composed of (100) surfaces is predicted only under the extreme conditions of (a) and (e), where the low-energy (100) surfaces have NaO and TaO_2 terminations, respectively. f) Na 1s, O 1s, and Ta 4f XPS peaks of the $NaTaO_3$ samples.

Ta-deficient/Na-deficient (i.e., O-rich) and Ta-rich/Na-deficient conditions, respectively. These endpoints approximate the conditions encountered in the synthesis using $TaO_x/NaNO_3$ and $Ta/NaNO_3$ precursors, respectively. We assume that, in both conditions, the Na species has the lowest possible chemical potential (–1.33 to –3.59 eV) due to being bound in the $NaNO_3$ precursor. The chemical potential of Ta is allowed to vary from being as deficient as possible in the TaO_x compound (–11.76 eV) to rich (0 eV) in the elemental Ta compound.

The computed surface energies and equilibrium particle shapes suggest that a cubic shape dominates in both Ta-rich/Na-deficient and Ta-deficient/Na-rich environments, which approximate the synthesis conditions while using $Ta/NaNO_3$ and TaO_x/NaAc precursors, respectively. In both situations, this shape is enabled by the stabilization of the (100) surface, albeit at different terminations. The Ta-rich (100)-TaO_2 surface termination and the (100)-NaO surface termination are stabilized with an estimated surface energy of 0.80 and 0.44 J m^{-2} under Ta-rich/Na-deficient conditions and Na-rich/Ta-deficient conditions, respectively (Tables S1 and S2, Supporting Information). The calculated energy for both possible (100) surfaces appears to match closely with the calculated energy in a previous study of cubic $NaTaO_3$ by Portugal et al.[29] (Table S3, Supporting Information).

In the Ta-rich/Na-deficient case, the corners of the (100) cube, however, appear to be truncated by (311) surfaces. We note that the presence of (311) surfaces is especially sensitive to the value of chemical potential of Na. For slightly lower values of chemical potential of Na, the (100)-TaO_2 surface energy is decreased even further and the (311) no longer appears in the calculated Wulff shape. The presence of some amount of (311) in Ta-rich conditions is not unreasonable, however, due to the surface's Ta termination.

As μ_{Ta} decreases along the rightmost boundary of the $NaTaO_3$ domain, the (210) and (221) surfaces decrease in energy and begin to appear in the computed Wulff shape. At the upper endpoint, the predicted Wulff shape is entirely composed of (210)-NaO, (221)-NaO, and (100)-NaO surfaces; the energies of these surfaces are shown in Table S4 (Supporting Information). The dominance of these surfaces can be attributed to their NaO terminations (which lack any Ta atoms).

In agreement with our experiments, the calculated cubic Wulff shape in Figure 3 for Ta-rich/Na-deficient conditions matches the observed shapes of the experimentally synthesized $NaTaO_3$ nanoparticles. It appears that the observed nanocubes consist almost entirely of low-energy (100), TaO_2-terminated surfaces. As previously mentioned, the presence of (311) truncated corners is very sensitive to the Na chemical potential, which may explain some of the disagreement on the extent to which the nanocubes are truncated. While the nanocube for the $Ta/NaNO_3$ synthesis was experimentally observed, we did not obtain as close of a match between the predicted and experimentally observed particle shapes for the $TaO_x/NaNO_3$ synthesis, in which a truncated pyramid shape was observed. We attribute at least some of this disagreement to the unknown role in which the substrate stabilizes preferred interfaces. Additionally, our theoretical model does not incorporate any solvation effects within an ionic flux. Nonetheless, the observation of angled surface facets in the nanopyramids suggests that at least some higher index surfaces are being observed. We hypothesize that the (210)-NaO and/or (221)-NaO surfaces are likely candidates for these observed surfaces.

Finally, at the upper left point in the $NaTaO_3$ domain, the computed Wulff shape is a perfect cube, composed of the Na-rich (100)-NaO surface that only exposes Na atoms to the environment. Micrographs of $NaTaO_3$ synthesized under Ta-deficient/Na-rich conditions using TaO_x/NaAc precursors show a flat surface, which is in apparent disagreement with this computed shape. It should be highlighted, however, that the Wulff shape construction is limited by its dimensionality in illustrating the preferred geometry of a compound grown as a film on a flat substrate. While this limitation prevents a direct comparison, we highlight that a perfectly cubic Wulff shape

and a substrate-grown film with a flat surface could both reflect a strict energetic preference for a single surface. In this view, we hypothesize that the flat surface resulting from the TaO_x/NaAc precursors is dominated by the (100)-NaO surface.

Next, surface sensitive X-ray photoelectron spectroscopy (XPS) was performed to characterize the elemental surface composition of $NaTaO_3$ (Figure S5, Supporting Information). Before the XPS analysis, the samples were sufficiently washed with warm water to ensure a clean surface without residual Na salts. Figure 3f shows the Na 1s, O 1s, and Ta 4f XPS peaks of the $NaTaO_3$ samples that exhibit different elemental ratio of Na, Ta, and O. The Na:Ta:O ratio was 8.4:25.0:66.6 for the nanocubes, 11.9:15.0:73.1 for the truncated pyramids, and 20.6:14.8, 64.6 for the thin films. These ratios agree with the results of our calculations and confirm that $NaTaO_3$ nanocubes, truncated pyramids, and thin films have Ta-rich, Na-deficient/Ta-deficient/O-rich, and Na-rich surface terminations, respectively. Together, our simulation and experimental results indicate that the shape and surface chemistry of $NaTaO_3$ films can be controlled through flux-mediated synthesis.

After exploring the shape evolution and surface chemistries of $NaTaO_3$, we evaluated the physical properties and band structure of $NaTaO_3$ depending on shape. The optical absorption properties of the different $NaTaO_3$ samples on quartz glass are shown in **Figure 4**a. The absorption edges of the $NaTaO_3$ samples are found ≈300 nm. Compared to the nanocubes, the truncated pyramids and the thin films show lower negligible visible light absorption, which means $NaTaO_3$ truncated pyramids and thin films are highly transparent to visible light. The bandgap energies of $NaTaO_3$ were found to be ≈4.1 eV (300 nm), extracted from Tauc plots of the absorbance spectra, Figure S6 (Supporting Information). XPS results confirmed that the $NaTaO_3$ nanocubes, truncated pyramids, and thin films exhibit *n*-type conductivity with a Fermi level located at 2.73, 2.81, and 2.75 eV above the valence band maximum, respectively (experimental section for details and Figure S7, Supporting Information). The calculated conduction band minimum (CBM), (and valence band maximum (VBM)), of the three different $NaTaO_3$ shapes were −4.10 (−8.19), −4.39 (−8.49), and −4.01 eV (−8.12 eV), respectively.

From energy level considerations, we anticipate that $NaTaO_3$ is a suitable electron transport material for halide perovskite solar cells (PSCs). Halide perovskite materials are highly promising for next generation optoelectronic devices including photovoltaics.[30–34] To date, electron extraction in PSCs is most widely achieved via TiO_2 and SnO_2.[35–38] Recently, solution-processed $NaTaO_3$ nanoparticles as an electron transport layer (ETL) have been reported in PSCs.[39] Ye et al. suggested an improvement in the efficiency of PSCs with $NaTaO_3$ through thickness control of the $NaTaO_3$ layer and in combination with a thin modified layer of phenyl-C61-butyric acid methyl ester between the perovskite and the $NaTaO_3$ layer.[39] Here however, we want to take advantage of the chemical tunability of $NaTaO_3$, and by targeted choice of their constituent elements, vary shape and surface composition and test their corresponding device performance. As illustrated in Figure 4b, the CBMs of

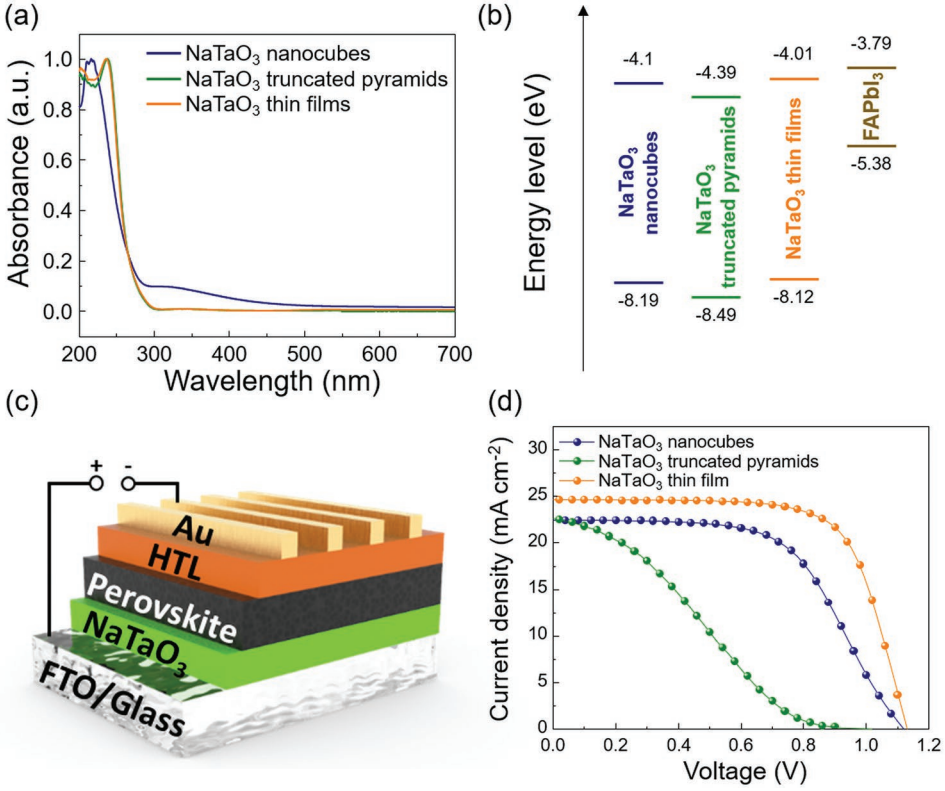

Figure 4. a) UV–vis absorption spectra of $NaTaO_3$ nanocubes, truncated pyramids, and thin films on quartz glass. b) Energy levels for $NaTaO_3$ layers and $FAPbI_3$. c) Device architecture of perovskite solar cells with $NaTaO_3$ as the electron transport layer. d) *J*–*V* curves of the PSCs with $NaTaO_3$ as ETL.

the $NaTaO_3$ samples are slightly lower than that of $FAPbI_3$ (–3.79 eV), and their VBMs are significantly lower than that of $FAPbI_3$ (–5.38 eV).[40] This energy alignment allows electrons to pass through smoothly, while it blocks holes. Using four-point probe, we found that the conductivity of $NaTaO_3$ nanocubes, truncated pyramids, and thin films are 1×10^{-3}, 7.87×10^{-4}, and 2×10^{-3} S cm^{-1}, respectively, which is comparable with previously reported electron transport layer materials (Figure S8, Supporting Information).[41]

To investigate the charge transport/extraction ability of $NaTaO_3$, we fabricated conventional n-i-p PSCs on FTO glass, with a $NaTaO_3$ layer as the ETL, $FAPbI_3$ as the photoactive layer, 2,2′,7,7′-Tetrakis(*N*,*N*′-di-pmethoxyphenylamine)-9,9′-spirobifluorene (Spiro-MeOTD) as the HTL, and gold as the metal back contact (Figure 4c, see Experimental Section). Figure 4d illustrates the current density–voltage (*J*–*V*) characteristics of the devices under AM1.5 G at 1-sun intensity. The device with $NaTaO_3$ thin film exhibits superior device performance with a V_{oc} of 1.13 V, a short circuit current density (J_{sc}) of 24.67 mA cm^{-2}, a fill factor (FF) of 70.68%, and a resulting power conversion efficiency (PCE) of 19.53%. Noteworty, the V_{oc} of 1.13 V was attained without any optimization or sophisticated interface treatment of the $NaTaO_3$ layer. In comparison, we previously attained a V_{OC} of 1.13–1.16 V using the same perovskite composition, but with an optimized SnO_2 transport layer treated with KCl or KOH.[40,42] The photovoltaic parameters (V_{oc}, J_{sc}, and FF) for the $NaTaO_3$ nanocube sample are 1.11 ± 0.1 V, 22.21 ± 0.16 mA cm^{-2}, and 59.21 ± 1.28, respectively, leading to PCE of 14.81 ± 0.46%. The $NaTaO_3$ truncated pyramids-based device has the lowest PCE of 4.2% (V_{oc} of 0.98 V, J_{sc} of 20.02 mA cm^{-2}, and FF of 68.92%). These results indicate that the ETL morphology correlated to the precursor chemistries during synthesis significantly affects the performance. Future works will focus on device optimization to further increase the device PCE, and also explore alternative applications for the $NaTaO_3$ thin films.

3. Conclusion

In summary, a flux-mediated synthesis method for $NaTaO_3$ is presented resulting in highly distinctive, substrate covering shapes via precursor chemistry variation at comparatively low temperatures. Depending on the precursor chemistries, different reactions and crystallization pathways occur during the flux-mediated synthesis as observed by in situ diffraction analysis resulting in $NaTaO_3$ nanocubes, truncated pyramids or smooth thin films. We further correlate synthesis conditions with shape evolution using density functional theory, chemical potential diagrams, surface energy calculations, and Wulff constructions. Experiment and calculations confirm distinct elemental surface termination with Ta-, O- or Na-rich surfaces for nanocubes, truncated pyramids, and thin films, respectively. $NaTaO_3$ is a stable and wide bandgap *n*-type semiconductor material with many different applications in photovoltaics and photo electrochemistry. In this work it was applied to PSCs as efficient electron transport layer resulting in conversion efficiencies of >19%. This result suggests that tuning the properties of ternary oxides using flux-mediated synthesis provides a promising path toward the discovery of novel, high performance materials for photo-driven applications.

4. Experimental Section

$NaTaO_3$ Film Fabrication: $NaTaO_3$ thin films were synthesized by flux-mediated synthesis method using a novel approach inspired by prior work of Suzuki et al.[26] Ta metal thin films and amorphous TaO_x thin films were used as Ta source and four different Na salts ($NaNO_3$, CH_3COONa, NaCl, and $Na_2S_2O_3$) were employed as both the Na source as well as the flux. Briefly, Ta or amorphous TaO_x thin films were deposited on Si or fluorine-doped tin oxide (FTO)-glass substrate. Before Ta or TaO_x deposition, the substrates were cleaned using detergent, acetone, and isopropanol, rinsed with deionized water, and dried with nitrogen. Ta and TaO_x thin films were deposited on the substrate using a radio frequency magnetron sputtering system (AJA International, Inc.). The thickness of the Ta and TaO_x thin films was controlled by deposition duration time. The Ta and TaO_x thin films were treated by air plasma cleaner for 5 min to make them hydrophilic. Then, 100 µL of 2 M Na salt in ethylene glycol solution was deposited by spin coating at 4000 rpm for 30 s. The resulting films were dried at 80 °C for 10 min. Finally, the Na salt-coated samples were annealed at 600 °C for 2 h in air.

Device Fabrication: The perovskite precursor solution was prepared by dissolving $FAPbI_3$ (889 mg mL^{-1}), $MAPbBr_3$ (33 mg mL^{-1}), and MACl (33 mg mL^{-1}) in a dimethylformamide (DMF)/dimethylsulfoxide (DMSO) mixed solvent (8:1 v/v). The perovskite was deposited on $NaTaO_3$/FTO glass at 4000 rpm for 20 s, where 0.2 mL of diethyl ether was dropped after 10 s, and then annealed at 150 °C for 10 min. Subsequently, spiro-MeOTAD solution (85.8 mg of spiroMeOTAD (p-OLED Corp) in 1 mL of chlorobenzene with 33.8 µL of 4-tert-butylpyridine and 19.3 µL of Li-TFSI (520 mg mL^{-1} in acetonitrile) solution) was dropped at 3000 rpm for 30 s. For the top electrode, 80 nm gold was thermally deposited at an evaporation rate of 0.5 A s^{-1}. For the anti-reflection coating, 150 nm MgF_2 was thermally deposited at an evaporation rate of 1 A s^{-1}.

Film Characterization: The morphological and structural characterization of the $NaTaO_3$ thin films were conducted with scanning electron microscopy (Quanta FEG 250, FEI) using an acceleration voltage of 10 kV. The crystalline structure of the $NaTaO_3$ thin films was analyzed by X-ray diffraction with a Rigaku Smartlab diffractometer using Cu Kα radiation. During the in situ XRD measurement, the samples were heated (30 °C min^{-1}), annealed at 650 °C for 15 min, and then cooled down to room temperature. XPS analysis was performed using a Kratos Axis Ultra spectrometer with a monochromatic Al Kα line at 1486.69 eV. XPS depth profiling was used to investigate the atomic composition of samples using an Ar ion gun with power 1 kV and 600 nA on a raster area of 7.8 mm^{-2}. The areas of the XPS spectra of each element were obtained by fitting Gaussian peaks after removing the secondary electron background, followed by normalization with corresponding atomic sensitivity factors. The valence band maximum (VBM) was found by a linear extrapolation of the leading edge of the valence band spectra. The conduction band minimum (CBM) was determined by subtracting the bandgap energies of $NaTaO_3$. The Fermi levels were calculated by subtracting the value determined by linear extrapolation of the secondary electron edge from the photon energy (21.22 eV).[43] The absorption spectra of $NaTaO_3$ thin films on quartz glasses and the transmittance spectra of $NaTaO_3$ thin films on FTO glasses were measured using an UV–vis photospectrometer (SolidSpec-3700, Shimadzu). Four-point probe measurements were performed to measure electric conductivity of $NaTaO_3$ layer on a glass substrate.

Surface Slab Generation: Surface slab models for $NaTaO_3$ were generated following the methodology of Sun and Ceder[44] and its implementation in pymatgen.[45] To avoid incurring the higher computational cost associated with the monoclinic structure, the cubic polymorph of $NaTaO_3$ was used here as an approximation, since the cubic and monoclinic structures differ only slightly. The higher symmetry cubic perovskite structure greatly reduced the number of slab

calculations required and a similar approach had been taken in previous surface studies of the monoclinic phase.[46] The atomic structure for bulk cubic $NaTaO_3$ was acquired from the Materials Project (MP) database (mp-4170).[47] The lattice parameter of the computed structure, 3.983 Å, reasonably matches the experimental lattice parameter of 3.929 Å (ICSD 28617). The slabs were generated up to a maximum Miller index of 3, with a minimum slab thickness of 15Å and a minimum vacuum size of 15 Å. All slabs were symmetric and nonstoichiometric, meaning that the overall composition differed from $NaTaO_3$ due to the different possible terminations. In total, 26 unique slabs were generated.

Density Functional Theory Calculation: Density functional theory (DFT) calculations of $NaTaO_3$ slabs were performed using the generalized gradient approximation (GGA) method formulated by Perdew–Burke–Ernzerhoff (PBE)[48] with projector augmented wave (PAW) pseudopotentials as implemented in the Vienna Ab initio Simulation Package (VASP, version 6.2.1).[49,50] The VASP input parameters and *K*-point settings were chosen as defined in the MPSurfaceSet class within pymatgen, including a plane wave energy cutoff of 400 eV and *K*-point reciprocal density of 50 $Å^{-3}$. Of the 26 original slabs, 13 were successfully converged and are included in the results. All 13 noncoverging calculations are associated with high-index surfaces (i.e., at least one Miller index of 3) and unfavorable configurations that would likely lead to high surface energies. Note that for all DFT calculated total energies, the oxygen correction of –0.687 eV per oxygen atom was also included, as recently fit by Wang et al.[51] While DFT errors in solid state thermochemistry were known to impact absolute energies, novel schemes adjusting the elemental energies to capture experimental trends can minimize those values to 50 meV per atom or less.[52–55] Such schemes can be adapted to include uncertainty analyses.[51] Furthermore, by virtue of being a relative quantity, surface energies incur less uncertainty than the bulk or slab energies do, separately. Indeed, Karim et al found that the calculated GGA/GGA+U equilibrium particle shapes of $LiMn_2O_4$ spinel were highly similar, despite the large differences in absolute surface energies.[56]

Chemical Potential Diagram Construction: The chemical potential diagram of the Na-Ta-O system was created following the methodology of Todd et al.[57] using the implementation in pymatgen. The energies of phases in the Na-Ta-O chemical system were acquired from the MP database (version 2021.11.10).[58] The chemical potential limits for the synthesis of $NaTaO_3$ were determined by taking the conditions along the boundaries of the stability domain of $NaTaO_3$ within the chemical potential diagram. Note that in a ternary compound such as $NaTaO_3$, only two chemical potentials were independent; hence this stability domain is 2D (i.e., a polygon) within 3D chemical potential space. All analyses were performed in formation energy space, such that the reference chemical potentials of the pure elements at their standard states was zero ($\mu_i = 0$).

Surface Energy and Wulff Shape Calculations: The surface energies were calculated using the approach for nonstoichiometric slabs described by Kramer & Ceder.[59] This could be generally summarized by the equation

$$\gamma = \frac{1}{2A}\left(E_{slab} - \sum_i N_i \mu_i\right) \quad (1)$$

where 2*A* is the surface area of both sides of the slab, $E_{slab}$is the total computed energy of the slab, and N_i is the number of atoms of species *i* in the slab with chemical potential μ_i The values of the chemical potentials are subject to the constraint

$$\sum_i n_i \mu_i = E_{bulk} \quad (2)$$

where E_{bulk} is the total energy of bulk $NaTaO_3$ containing $n_i$atoms of each species *i*. This constraint was incorporated automatically by only assigning chemical potentials within the stability domain of $NaTaO_3$ as determined by the Na-Ta-O chemical potential diagram.

Wulff shapes were calculated following the methodology of Tran et al.[60] using the implementation in pymatgen. The Wulff shapes were determined at various points within the chemical potential stability domain of $NaTaO_3$. For each coordinate within the stability domain, surface energies were recalculated using the chemical potentials corresponding to that point's coordinates.

Device Characterization: The current density and voltage curves of the devices were measured with a Keithley 2401 source meter under simulated one sun AM 1.5G spectrum illumination (100 mW cm^{-2}) from an Oriel Sol3A class AAA solar simulator (Newport). The light intensity was first calibrated with a NREL-certified Si photodiode with a KG-5 filter. All devices were measured in ambient air with a 0.100 cm^2 sized metal aperture used to precisely define the active area during measurement. Devices were measured at a scan rate of 0.1 V s^{-1} from 1.2 to –0.1 V or 0.1 to 1.2 V in 0.02 V steps.

Supporting Information

Supporting Information is available from the Wiley Online Library or from the author.

Acknowledgements

K.H. acknowledges the Overseas Postdoctoral Fellowship of Basic Science Research Program (2021R1A6A3A03039891) through the National Research Foundation of Korea (NRF) and Basic Science Research Capacity Enhancement Project through Korea Basic Science Institute (National research Facilities and Equipment Center) grant (2019R1A6C1010024) funded by the Ministry of Education. S.T., T.H., and Y.Y. acknowledge support from the U.S. Department of Energy's Office of Energy Efficiency and Renewable Energy (EERE) under the Solar Energy Technologies Office under award number DE-EE0008751. T.K. thanks the German Research Foundation (DFG) for funding (fellowship number KO6414). Synthesis and characterization of sodium tantalate were performed at the Joint Center for Artificial Photosynthesis, a DOE Energy Innovation Hub, supported through the Office of Science of the U.S. Department of Energy under Award Number DE-SC0004993. F.B., S.S., and F.M.T. acknowledge Liquid Sunlight Alliance, which was supported by the U.S. Department of Energy, Office of Science, Office of Basic Energy Sciences, and Fuels from Sunlight Hub under Award Number DE-SC0021266. Work at the Molecular Foundry was supported by the Office of Science, Office of Basic Energy Sciences, of the U.S. Department of Energy under Contract No. DE-AC02-05CH11231. This manuscript was prepared with support from the Laboratory Directed Research and Development (LDRD) program of Lawrence Berkeley National Laboratory under U.S. Department of Energy Contract DE-AC02-05CH11231 (F.M.T. and C.M.S.-F.). 2D diffraction images were obtained at the Advanced Light Source, a U.S. DOE Office of Science User Facility under contract no. DE-AC02-05CH11231.

Conflict of Interest

The authors declare no conflict of interest.

Author Contributions

K.H. and S.T equally contributed to this work. C.M.S.-F. and K.H. conceived the idea. K.H. performed the $NaTaO_3$ synthesis and characterization. T.K. helped with GIWAX analysis. S.T. and T.H. fabricated and characterized perovskite solar cells supervised by Y.Y. M.J.M. M.G. and K.A.P. developed the theory. F.B., S.S., and F.M.T. helped to perform structural analysis and data validation. K.H., C.M.S.-F., and S.T. wrote the manuscript. All authors discussed the results and revised the paper.

Data Availability Statement

The data that support the findings of this study are available from the corresponding author upon reasonable request.

Keywords

charge transport layers, crystallization pathways, flux-mediated syntheses, perovskite solar cells, surface chemistry

Received: June 10, 2022
Revised: August 2, 2022
Published online:

[1] E. Bugaris, H.-C. zur Loye, *Angew. Chem., Int. Ed.* **2012**, *51*, 3780.
[2] J. Boltersdorf, N. King, P. A. Maggard, *Cryst. Eng. Comm.* **2015**, *17*, 2225.
[3] M. Brahlek, A. S. Gupta, J. Lapano, J. Roth, H.-T. Zhang, L. Zhang, R. Haislmaier, R. Engel-Herbert, *Adv. Funct. Mater.* **2018**, *28*, 1702772.
[4] H.-U. Habermeier, *Mater. Today* **2007**, *10*, 34.
[5] J. Honig, *Preparation and characterization of materials*, Academic Press, New York, USA **1981**.
[6] K. Vidyasagar, J. Gopalakrishnan, C. N. R. Rao, *Inorg. Chem.* **1984**, *23*, 1206.
[7] C. N. R. Rao, K. Biswas, *Essentials of inorganic materials synthesis*, John Wiley & Sons, Inc, Hoboken, NJ **2015**.
[8] M.-A. Einarsrud, T. Grande, *Chem. Soc. Rev.* **2014**, *43*, 2187.
[9] D. Elwell, B. W. Neate, *J. Mater. Sci.* **1971**, *6*, 1499.
[10] X. Liu, N. Fechler, M. Antonietti, *Chem. Soc. Rev.* **2013**, *42*, 8237.
[11] D. Liu, S. Li, P. Zhang, Y. Wang, R. Zhang, H. Sarvari, F. Wang, J. Wu, Z. Wang, Z. D. Chen, *Nano Energy* **2017**, *31*, 462.
[12] P. Tiwana, P. Docampo, M. B. Johnston, H. J. Snaith, L. M. Herz, *ACS Nano* **2011**, *5*, 5158.
[13] Z. Cao, C. Li, X. Deng, S. Wang, Y. Yuan, Y. Chen, Z. Wang, Y. Liu, L. Ding, F. Hao, *J. Mater. Chem. A* **2020**, *8*, 19768.
[14] Y. Zhou, X. Li, H. Lin, *Small* **2020**, *16*, 1902579.
[15] H. Tan, A. Jain, O. Voznyy, X. Lan, F. P. G. d. Arquer, J. Z. Fan, R. Quintero-Bermudez, M. Yuan, B. Zhang, Y. Zhao, F. Fan, P. Li, L. N. Quan, Y. Zhao, Z.-H. Lu, Z. Yang, S. Hoogland, E. H. Sargent, *Science* **2017**, *355*, 722.
[16] J. K. Yang, B. Liang, M. J. Zhao, Y. Gao, F. C. Zhang, H. L. Zhao, *Sci. Rep.* **2015**, *5*, 15001.
[17] W. Y. Lee, Y. W. Bae, D. E. Stinton, *J. Am. Ceram. Soc.* **1995**, *78*, 1927.
[18] A. K. Singh, J. H. Montoya, J. M. Gregoire, K. A. Persson, *Nat. Commun.* **2019**, *10*, 443.
[19] P. Zhang, J. Zhang, J. Gong, *Chem. Soc. Rev.* **2014**, *43*, 4395.
[20] L. Polak, J. H. Rector, M. J. Slaman, R. J. Wijngaarden, *J. Phys. Chem. C* **2016**, *120*, 23559.
[21] C.-C. Hu, H. Teng, *Appl. Catal. A* **2007**, *331*, 44.
[22] F.-F. Li, D.-R. Liu, G.-M. Gao, B. Xue, Y.-S. Jiang, *Appl. Catal. B* **2015**, *166*, 104.
[23] S. Lee, K. Teshima, Y. Mizuno, K. Yubuta, T. Shishido, M. Endo, S. Oishi, *Cryst. Eng. Comm.* **2010**, *12*, 2871.
[24] D. G. Porob, P. A. Maggard, *J. Solid State Chem.* **2006**, *179*, 1727.
[25] W.-H. Lin, C. Cheng, C.-C. Hu, H. Teng, *Appl. Phys. Lett.* **2006**, *89*, 211904.
[26] S. Suzuki, K. Teshima, K. Yubuta, S. Ito, Y. Moriya, T. Takata, T. Shishido, K. Domen, S. Oishi, *Cryst. Eng. Comm.* **2012**, *14*, 7178.
[27] Q. Zhang, Z. Li, S. Wang, R. Li, X. Zhang, Z. Liang, H. Han, S. Liao, C. Li, *ACS Catal.* **2016**, *6*, 2182.
[28] J. Shi, G. Liu, N. Wang, C. Li, *J. Mater. Chem.* **2012**, *22*, 18808.
[29] G. R. Portugal, S. F. Santos, J. T. Arantes, *Appl. Surf. Sci.* **2020**, *502*, 144206.
[30] S. D. Stranks, H. J. Snaith, *Nat. Nanotechnol.* **2015**, *10*, 391.
[31] M. Grätzel, *Nat. Mater.* **2014**, *13*, 838.
[32] N.-G. Park, M. Grätzel, T. Miyasaka, K. Zhu, K. Emery, *Nat. Energy* **2016**, *1*, 16152.
[33] W. Zhang, G. E. Eperon, H. J. Snaith, *Nat. Energy* **2016**, *1*, 16048.
[34] M. A. Green, S. P. Bremner, *Nat. Mater.* **2017**, *16*, 23.
[35] L. Xiong, M. Qin, G. Yang, Y. Guo, H. Lei, Q. Liu, W. Ke, H. Tao, P. Qin, S. Li, H. Yu, G. Fang, *J. Mater. Chem. A* **2016**, *4*, 8374.
[36] T. Leijtens, G. E. Eperon, S. Pathak, A. Abate, M. M. Lee, H. J. Snaith, *Nat. Commun.* **2013**, *4*, 2885.
[37] B. Roose, J.-P. C. Baena, K. C. Gödel, M. Graetzel, A. Hagfeldt, U. Steiner, A. Abate, *Nano Energy* **2016**, *30*, 517.
[38] G. Yang, C. Chen, F. Yao, Z. Chen, Q. Zhang, X. Zheng, J. Ma, H. Lei, P. Qin, L. Xiong, W. Ke, G. Li, Y. Yan, G. Fang, *Adv. Mater.* **2018**, *30*, 1706023.
[39] Q.-Q. Ye, M. Li, X.-B. Shi, M.-P. Zhuo, K.-L. Wang, F. Igbari, Z.-K. Wang, L.-S. Liao, *ACS Appl. Mater. Interfaces* **2020**, *12*, 21772.
[40] S. Tan, T. Huang, I. Yavuz, R. Wang, M. H. Weber, Y. Zhao, M. Abdelsamie, M. E. Liao, H.-C. Wang, K. Huynh, K.-H. Wei, J. Xue, F. Babbe, M. S. Goorsky, J.-W. Lee, C. M. Sutter-Fella, Y. Yang, *J. Am. Chem. Soc.* **2021**, *143*, 6781.
[41] H. Pan, X. Zhao, X. Gong, H. Li, N. H. Ladi, X. L. Zhang, W. Huang, S. Ahmad, L. Ding, Y. Shen, M. Wang, Y. Fu, *Mater. Horiz.* **2020**, *7*, 2276.
[42] S. Tan, T. Huang, I. Yavuz, R. Wang, T. W. Yoon, M. Xu, Q. Xing, K. Park, D.-K. Lee, C.-H. Chen, R. Zheng, T. Yoon, Y. Zhao, H.-C. Wang, D. Meng, J. Xue, Y. J. Song, X. Pan, N.-G. Park, J.-W. Lee, Y. Yang, *Nature* **2022**, *605*, 268.
[43] K. Hong, K. C. Kwon, K. S. Choi, Q. V. Le, S. J. Kim, J. S. Han, J. M. Suh, S. Y. Kim, C. M. Sutter-Fella, H. W. Jang, *J. Mater. Chem. C* **2021**, *9*, 15212.
[44] W. Sun, G. Ceder, *Surf. Sci.* **2013**, *617*, 53.
[45] S. P. Ong, W. D. Richards, A. Jain, G. Hautier, M. Kocher, S. Cholia, D. Gunter, V. L. Chevrier, K. A. Persson, G. Ceder, *Comput. Mater. Sci.* **2013**, *68*, 314.
[46] X. Liu, K. Sohlberg, *Comput. Mater. Sci.* **2015**, *103*, 1.
[47] L. Zhao, R. A. Kerner, Z. Xiao, Y. L. Lin, K. M. Lee, J. Schwartz, B. P. Rand, *ACS Energy Lett.* **2016**, *1*, 595.
[48] J. P. Perdew, K. Burke, M. Ernzerhof, *Phys. Rev. Lett.* **1996**, *77*, 3865.
[49] G. Kresse, J. Furthmüller, *Phys. Rev. B* **1996**, *54*, 11169.
[50] P. E. Blöchl, *Phys. Rev. B* **1994**, *50*, 17953.
[51] A. Wang, R. Kingsbury, M. McDermott, M. Horton, A. Jain, S. P. Ong, S. Dwaraknath, K. A. Persson, *Sci. Rep.* **2021**, *11*, 15496.
[52] A. Jain, G. Hautier, S. P. Ong, C. J. Moore, C. C. Fischer, K. A. Persson, G. Ceder, *Phys. Rev. B* **2011**, *84*, 045115.
[53] R. Friedrich, D. Usanmaz, C. Oses, A. Supka, M. Fornari, M. Buongiorno Nardelli, C. Toher, S. Curtarolo, *npj Comput. Mater.* **2019**, *5*, 59.
[54] V. Stevanović, S. Lany, X. Zhang, A. Zunger, *Phys. Rev. B* **2012**, *85*, 115104.
[55] M. Aykol, C. Wolverton, *Phys. Rev. B* **2014**, *90*, 115105.
[56] A. Karim, S. Fosse, K. A. Persson, *Phys. Rev. B* **2013**, *87*, 075322.
[57] P. K. Todd, M. J. McDermott, C. L. Rom, A. A. Corrao, J. J. Denney, S. S. Dwaraknath, P. G. Khalifah, K. A. Persson, J. R. Neilson, *J. Am. Chem. Soc.* **2021**, *143*, 15185.
[58] A. Jain, S. P. Ong, G. Hautier, W. Chen, W. D. Richards, S. Dacek, S. Cholia, D. Gunter, D. Skinner, G. Ceder, K. A. Persson, *APL Mater.* **2013**, *1*, 011002.
[59] D. Kramer, G. Ceder, *Chem. Mater.* **2009**, *21*, 3799.
[60] R. Tran, Z. Xu, B. Radhakrishnan, D. Winston, W. Sun, K. A. Persson, S. P. Ong, *Sci. Data* **2016**, *3*, 160080.